J. Fluid Mech. (1996), *vol.* 329, *pp.* 309–339

Surface ripples due to steady breaking waves

By JAMES H. DUNCAN AND ATHANASSIOS A. DIMAS

Department of Mechanical Engineering, University of Maryland, College Park, MD 20742, USA

(Received 12 February 1996 and in revised form 25 July 1996)

Breaking waves generated by a two-dimensional hydrofoil moving near a free surface at constant speed (U_∞), angle of attack and depth of submergence were studied experimentally. The measurements included the mean and fluctuating shape of the breaking wave, the surface ripples downstream of the breaker and the vertical distribution of vertical and horizontal velocity fluctuations at a single station behind the breaking waves. The spectrum of the ripples is highly peaked and shows little variation in both its peak frequency and its shape over the first three wavelengths of the wavetrain following the breaker. For a given speed, as the breaker strength is increased, the high-frequency ends of the spectra are nearly identical but the spectral peaks move to lower frequencies. A numerical instability model, in conjunction with the experimental data, shows that the ripples are generated by the shear flow developed at the breaking region. The spectrum of the vertical velocity fluctuations was also found to be highly peaked with the same peak frequency as the ripples, while the corresponding spectrum of the horizontal velocity fluctuations was found not to be highly peaked. The root-mean-square (r.m.s.) amplitude of the ripples (η_{rms}) increases with increasing speed and with decreasing depth of submergence of the hydrofoil, and decreases as $x^{-1/2}$ with increasing distance x behind the breaker. The quantity $(g\eta_{rms})/(U_\infty V_{rms})$ (where V_{rms} is the maximum r.m.s. vertical velocity fluctuation and g is the gravitational acceleration) was found to be nearly constant for all of the measurements.

1. Introduction

Steady breaking waves are found in the wave system of ships. These breakers convert kinetic and potential energy from the wave system into kinetic energy in the turbulent wakes of the breakers. Baba (1969) has shown that these turbulent wakes are momentum deficient, like the wake of a towed body. In some cases, the drag due to breaking was found to account for as much as 15% of the total drag on the ship. Ship-generated breaking waves are also of interest because of their role in ship-wake detection by synthetic aperture radar (SAR) images of the ocean surface. Along the centreline of the ship path, the SAR images appear dark indicating that there is a deficit of short surface waves in that region. The width of this dark region includes the width of the breakers at the bow and stern of the ship. The first step in understanding the interaction between the breaker system and the existing wind waves that brings about this short-wave deficit is to understand the breakers and their wakes as the ship advances through calm water.

In order to gain insight into the dynamics of ship-generated and other types of breaking waves, a number of investigators have studied small-scale breaking waves generated by two-dimensional, fully submerged hydrofoils moving at constant depth

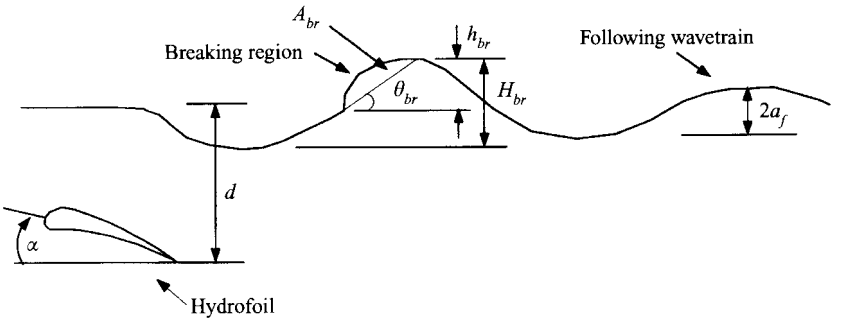

FIGURE 1. Schematic showing the hydrofoil, the breaking wave and the definitions of various geometrical quantities.

(d), speed (U_∞) and angle of attack (α), see figure 1. This flow is simpler than the ship wave system because it is two-dimensional in the mean and because the viscous wake of the hydrofoil is well below the wake of the breaker, while the viscous wake of the ship is intertwined with the breakers and their wakes. The research into these waves can be divided into two areas: the overall dynamics of the waves and the surface height fluctuations. In the area of overall dynamics, the important issues include the determination of incipient breaking conditions, the drag produced by the breakers, the mechanism that creates the drag, the energy dissipated, and the mean wave shape. In the area of surface height fluctuations, the important issues include the generation mechanism, the amplitude, frequency and wavelength, and the propagation of these disturbances in the wake.

The first papers on the overall dynamics of the breaker and wake system were published by Battjes & Sakai (1981) and Duncan (1981, 1983*a*, *b*). The following description of the physics of this flow is based on these early studies. There are two components of the drag on the hydrofoil as measured from the flow field far downstream. The first is due to the viscous wake of the foil. This wake is thin near the trailing edge of the foil and grows vertically, eventually reaching the surface far downstream. The second component of the drag is due to the steady wavetrain that the foil generates. If the waves are not breaking, the drag associated with the free surface can be computed from measurements of the foil speed and the amplitude of the waves (Duncan 1983*b*). The amplitude of the non-breaking wavetrain increases as d is decreased or α is increased. When d is small enough or α is large enough, the first wave behind the foil breaks and the amplitude of the following (residual) wavetrain decreases. This amplitude decreases further as the breaker strength is increased by decreasing d or increasing α. Under breaking conditions, the drag of the foil due to the effect of the free surface has two components: one due to the turbulent viscous wake of the breaker and the other due to the residual non-breaking wavetrain. Battjes & Sakai (1981) measured mean velocity and turbulence characteristics in the wakes of two breakers with flow speeds of 108 and 66 cm s^{-1}. They found the wake to behave much like the half-wake of a two-dimensional body in an infinite fluid. The total drag on the foil due to surface effects was found by Duncan (1983*a*) (U_∞ ranging from 60 to 100 cm s^{-1}) to have values as high as 3 times the maximum drag, R_{max}, that could be found theoretically with a non-breaking wavetrain. However, at the point of incipient breaking, the drag on the hydrofoil was about $0.8R_{max}$. For resistances greater than $0.8R_{max}$ but less than $1.0R_{max}$, it was found that the wave could exist in either a breaking or a non-breaking state. The wave slope at the

point of incipient breaking was found to be about 17°. A theoretical analysis of steady breakers was presented by Cointe & Tulin (1994). In this work, the breaker is modelled as an essentially stagnant zone riding on the forward face of the wave and the interaction of this region with the underlying flow is modelled with mixing-layer theory. Many important aspects of the physics of steady breakers, their wakes and the following wavetrain were elucidated in this insightful study. In two recent studies, Lin & Rockwell (1994, 1996) measured instantaneous flow fields using particle image velocimetry in several breaking waves (U_∞ ranging from 33.4 to 48.2 cm s^{-1}). The results showed that the turbulent zone on the forward face of the wave (defined herein as the breaking region) was essentially stagnant in a frame of reference moving with the wave. This is in agreement with the speculations of previous researchers (see for instance Duncan 1981 and the theoretical model of Cointe & Tulin 1994).

Two important studies of surface height fluctuations were reported by Banner & Fooks (1985) and Walker *et al.* (1996). Banner & Fooks (1985) generated two breaking waves (wavelengths of 0.2 m and 0.33 m) in a recirculating water channel and measured two-point surface-height time-series data with wire-type gauges placed in the breaking wave both upstream and downstream of the crest. Radar returns from these breakers were also measured. From these measurements, they presented the spectra of surface height fluctuations at single points along the crest, two-point correlation functions in the breaking region in both the streamwise and cross-stream directions, and wavenumber spectra in the streamwise direction within the breaking region. They found that the frequency spectra at all spatial locations showed the same peak frequency in a given wave and that this frequency decreased with the wavelength of the breaker. The wavelength of these fluctuations increased with the wavelength of the breaker. These disturbances were found to propagate downstream.

More recently, Walker *et al.* (1996) studied surface ripples on waves generated with a submerged hydrofoil in a recirculating water channel. They used a single flow speed of 108 cm s^{-1} and studied three waves of different breaking strengths by varying the angle of attack of the foil. Surface shape measurements in the breaking region and in the wake were made photographically with a laser light sheet (aligned with the flow direction) and a video camera. The temporal sampling rate of this system was 30 images per second and the spatial resolution was 0.8 mm in the horizontal and vertical. The breaker strength was quantified by using the flux of energy in the wake, which was obtained from measurements of distributions of mean flow and total head. Radar returns from these breakers were also measured. It was found that the variance in surface height fluctuations was largest at the breaking region and decreased rapidly with distance behind the breaking wave crest. The temporal frequency of these fluctuations was low at the toe of the breaker and about 50 rad s^{-1} further back on the breaker. This frequency remained constant with distance downstream in the wake. The variation of these frequencies with breaker strength was not reported, presumably because of the rather low temporal sampling frequency used in this work. It was also found that the wavenumber of the ripples decreased with distance downstream. The fact that the frequency was constant with distance downstream, while the amplitude and wavenumber decreased, led the authors to speculate that the ripples were behaving like surface waves propagating on a spatially varying current, which has speeds ranging from 0 at the breaking region to 108 cm s^{-1} in the far wake. A simple calculation using conservation of wave action and deep-water wave theory was used to predict the change in ripple amplitude between the breaking region and rear face of the breaking wave. This calculation gave fairly accurate results in spite of the strong shear that exists in these regions of the flow.

In the present paper, the free-surface fluctuations and turbulence generated by a hydrofoil-produced steady breaking wave are studied. The emphasis is on understanding the physical processes that create the surface height fluctuations and their connection to the overall dynamics of the mean flow. Measurements are reported for five breaking waves encompassing three flow speeds (60, 80 and 100 cm s^{-1}). In the area of the breaking region, the mean and fluctuating free-surface shape are measured from photographs, while in the wake the surface fluctuations are measured at several streamwise locations with an optical wave-height gauge. The wave-height gauge used here measures water height versus time at only a single point but does so with better accuracy and higher temporal resolution than the method used by Walker *et al.* (1996). Thus, the variations of ripple properties with breaker conditions are reported herein. In addition to these surface shape measurements, the distribution of turbulence properties with depth at fixed streamwise locations are measured with hot-film X-probes. Preliminary results from the above measurements were reported by Duncan (1993). In order to interpret the data resulting from the above measurements, the numerical model of instabilities of a shear flow with a free surface developed by Triantafyllou & Dimas (1989) is employed. In particular, the numerical model is able to shed light on the generation source of the ripples and their frequency-wavelength characteristics.

A description of the measurement and data reduction techniques is given in §2. This is followed in §3 by a description of the experimental results of the study. These results are discussed in the light of the numerical model in §4. Finally, the conclusions of the work are given in §5.

2. Experimental set-up and data reduction

2.1. *The wave tank and the hydrofoil*

The experiments were performed in a towing tank at Quest Integrated, Inc. The tank is 18 m long, 1.2 m wide and 0.9 m deep (figure 2). The walls are made of glass for flow visualization purposes. The hydrofoil rides on two tracks mounted from the bottom of the tank near the sidewalls. An instrument carriage rides on a separate set of tracks mounted outside the tank. Both the hydrofoil and the instrument carriage are propelled by towing wires that are driven by a single variable-speed AC motor. Towing speeds up to 1.2 m s^{-1} can be achieved with this system. The towing wires for the hydrofoil enter the water at one end of the tank and leave the water at the other end. Thus, no part of the towing system pierces the water surface in the vicinity of the hydrofoil.

The hydrofoil is made of aluminium and has an FX 63-137, Wortmann profile smoothed by Eppler (Marchman & Abtahi 1985) with a chord of 18.14 cm. The foil spans the width of the tank with a clearance of about 0.5 cm between the edges of the foil and the glass walls of the tank. The foil is mounted on two half-inch-thick nylon blocks placed 2.5 cm from its ends. Two grooves in each block provide bearing surfaces for the foil to slide along the tracks at either a 10° or a 5° angle of attack. The distance from the trailing edge of the foil to the bottom of the tank was 47.0 cm and 49.3 cm for the 5° and 10° angles of attack, respectively. The depth of submergence of the foil was then varied by changing the height of the water. In all cases, the wavelength of the waves, $2\pi U_\infty^2/g$ (as calculated from linear deep-water wave theory), was greater than the total water depth. Thus, the breakers can be considered as deep-water waves. From visual observations of the breaking waves, it

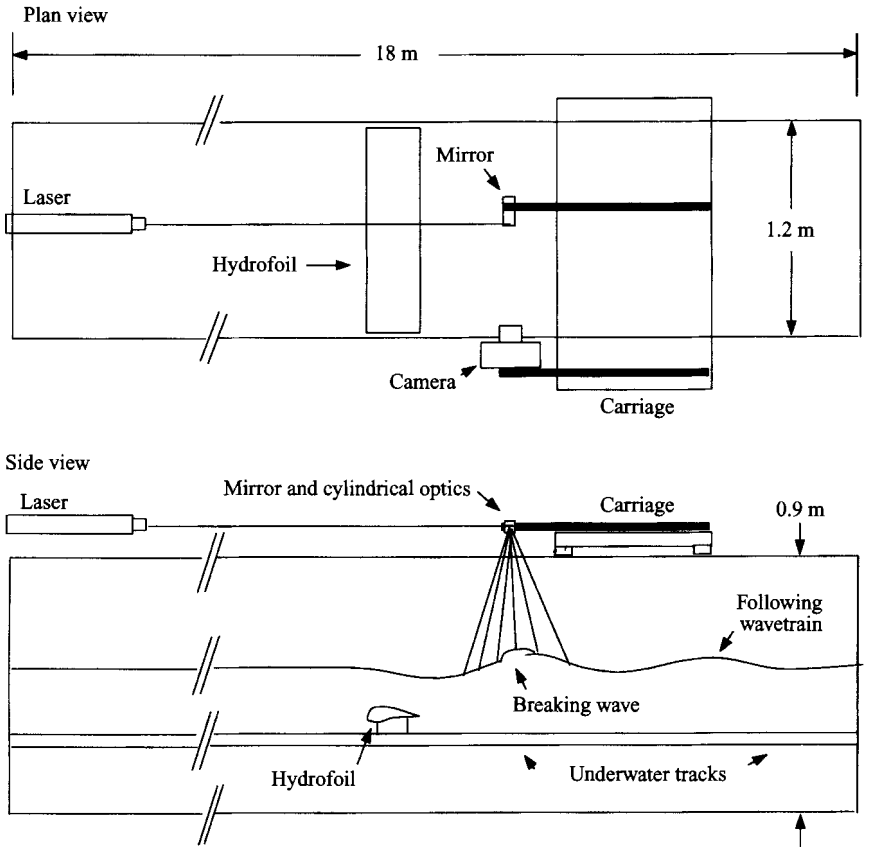

FIGURE 2. Schematic showing the configuration of the tank, carriage, optics and hydrofoil for photographing the breaking region. Similar set-ups were used for the measurements of the surface ripples and turbulence in the wake.

appeared that the flow produced by this system was two-dimensional in the middle 0.6 m of the tank. All measurements were taken along the tank centreline.

The tracks for the instrument carriage consist of a 0.1 m diameter stainless steel pipe on one side of the tank and 0.05 m wide flat bronze surface on the other. The carriage is mounted on four oil shoes in a manner such that it rides along the tracks on a film of oil that is roughly 0.2 mm in thickness. This system provides an extremely low vibration level which is essential for making the surface height measurements reported below. It was thought that contamination of the water surface with oil from the carriage bearing system might affect the breaking waves. Fortunately, it was easy to see even small amounts of oil on the water surface, and none was found during the present experiments. To be sure that the water surface was relatively clean, it was skimmed periodically by moving a barrier along the tank and removing the compressed surface layer that resulted from this process. Also, the surface tension was measured periodically with a capillary rise tube and found to be very close to that of clean water in all cases.

2.2. *Wave profile measurement technique*

The profiles of the breaking waves were measured from 35 mm photographs. To obtain the photographs, a laser light sheet and a 35 mm motorized Nikon F2 camera were mounted on the towing carriage which was set to move along with the wave. A

schematic diagram of the set-up is shown in figure 2. The camera was positioned to view the wave from the side and slightly above the water surface. The light sheet was formed from a 5 W Argon-Ion laser that was mounted at the end of the tank. The laser beam was reflected off a mirror on the carriage to a rotating prism. This system created a light sheet of approximately 1 mm in thickness oriented vertically along the centreline of the tank. Fluorescein dye was mixed with the water to a concentration of about 5 p.p.m. The wavelength of maximum excitation of the dye is 491 nm while the wavelength of maximum emission is 524 nm. Thus, the dye within the light sheet radiated greenish-yellow light and the camera recorded a picture of the wave profile at the centreline of the tank. An optical filter was placed on the camera so that any light coming directly from the laser was rejected. This prevented specular reflections from the water surface from appearing in the photographs. The motorized camera took 3.5 photographs per second: thus during a single run about 30 photographs were taken. Two light-emitting diodes were placed 20 cm apart at the same height above the water surface to provide registration points in each frame in the sequence.

In the data reduction process, each photograph was first digitized from a CCD (charge-coupled-device) camera image of the photograph and the digitized image was stored on an engineering workstation. The digitized image was in black and white with 256 grey levels per pixel and an approximate image size of 512 by 512 pixels. Next, the water surface was located as the boundary between the dark pixels above the water surface and the light pixels below the water surface. Drops of water above the water surface were ignored by the computer program. The wave profile from each image was then smoothed by a running average filter to remove evidence of the digitization. The wave profiles were then stored for processing as described in §3.2.

2.3. *Laser wave-height gauge*

A laser wave-height gauge (Lin & Liu 1982) was used to make measurements of the height of the water surface versus time at a spatial point that was either fixed in laboratory coordinates or moved in a manner that maintained a fixed position relative to the hydrofoil. The measurement system is shown schematically in figure 3.

As in the breaker profile measurements, the laser was placed at the end of the tank and the laser beam was pointed horizontally along the centreline of the tank above the water surface. A system of mirrors and collimators on the carriage focused the light beam and redirected it perpendicular to the water surface. The water was dyed with Fluorescein dye at a concentration of about 5 p.p.m. A line-scan camera (Reticon L-1024) viewed the intersection of the light beam and the water surface from the side and slightly above the water surface. The camera contains an array of 1024 light-sensitive elements and was oriented so that the array was in the vertical plane made up by the light beam and the line of sight of the camera. The light-sensitive elements that viewed the air above the water surface received little light. The elements that viewed the water received light from the glowing dye. Software within the camera controller determined the number of the light-sensitive elements (from 0 to 1023) that were at the boundary between the dark elements above the water surface and the light elements below. The number was then recorded by the computer. The entire linear array was read approximately every 0.001 s. The actual digitization rate varied slightly from run to run and was measured with a counter and recorded. Calibration of the gauge was achieved by moving the camera vertically over known distances while it viewed an undisturbed water surface in the tank. About five data points were obtained in this way and a least-squares fit of a second-order polynomial to the calibration points was performed. The curve of height versus element number is

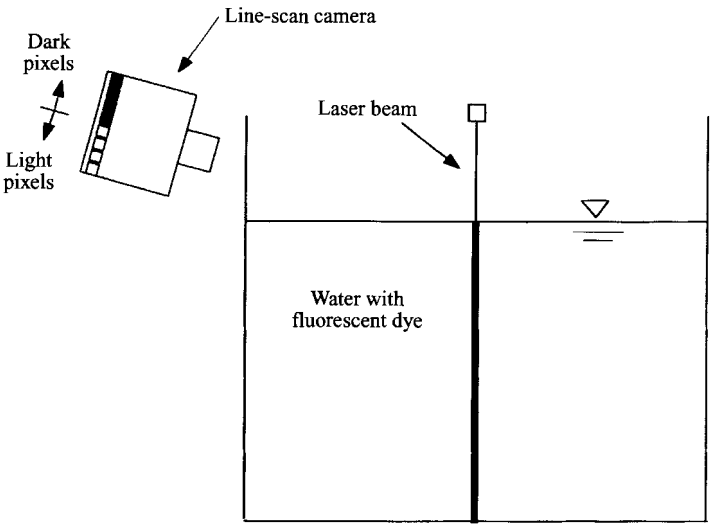

FIGURE 3. Schematic showing laser wave-height gauge. The air–water interface is tracked as the boundary between the pixels that image the laser beam in the air and those that image the laser beam in the water which is mixed with fluorescent dye.

slightly nonlinear due to the effects of lens distortion and camera angle which are adequately accounted for by the second-order term in the polynomial.

The system described above was used to measure the wavetrain following the hydrofoil and the small-scale ripples in the wake of the breaker. In order to measure the following wavetrain, the instrument carriage was positioned at a fixed point near the centre of the tank. In this case, the camera and lenses were arranged so that the height range of the camera was about 4 cm with a resolution of about 0.04 mm. The light-sensitive elements are about 17 times wider than the element to element spacing. Thus, the width of the spot examined by the camera was about 0.68 mm. In order to measure the ripples generated by the breaker, the instrument carriage was moved with the hydrofoil so that the wave-height gauge measured the surface height versus time at a position fixed with respect to the hydrofoil. In this case, the camera position and lenses were arranged to give a height range of about 2 cm, a resolution of about 0.02 mm and a measurement width of about 0.34 mm. For this instrument to make accurate measurements, it is important that the variation of the water surface height in the measurement width be much less than the height corresponding to one light-sensitive element in the camera (0.02 mm). The smallest wavelengths of the ripples on the breaking region (measured from photographs) were found to be 3.2 cm. The theoretical and data analysis given later in this paper indicates that this wavelength increases as the wave propagates through the wake. Thus, the measuring width of the laser wave-height gauge, which is used in the wake, is no bigger than about 0.01 times the wavelength of the dominant ripples. The measured amplitudes of these waves are on the order of 1 mm in the wake. The above amplitude and wavelength indicate that the surface height variation over the measurement width is about 0.001 mm. This variation is sufficiently small to ensure accurate surface height measurements.

In order to assess the noise level of this measurement system, a data run was taken while moving over a flat water surface (no hydrofoil). The measured height fluctuations, which included the effects of carriage vibration and electronics, had an

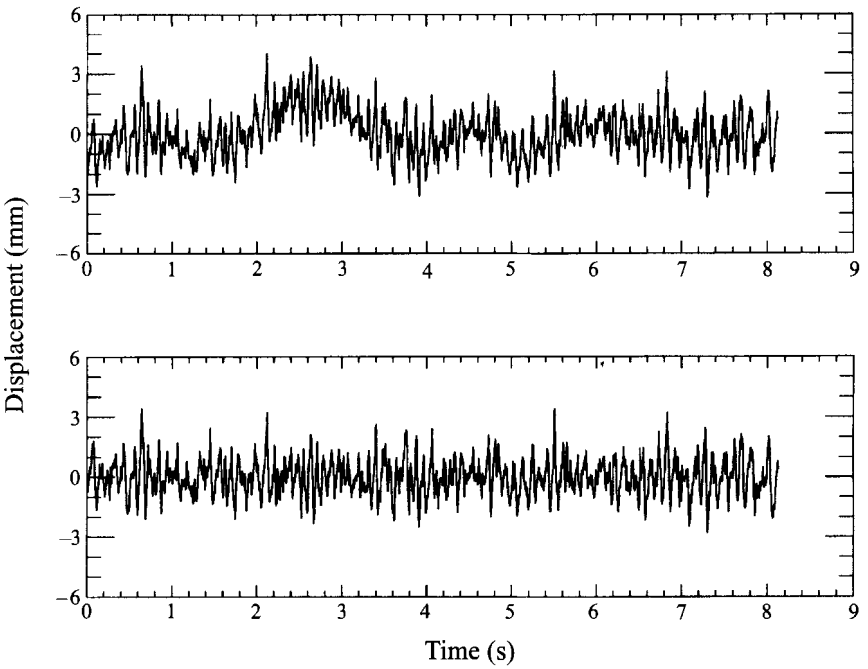

FIGURE 4. Surface displacement versus time: $U_\infty = 80$ cm s^{-1}, $\alpha = 10°$, $d = 28.7$ cm. The upper plot is raw data and the lower plot is the data after high-pass filtering.

r.m.s. level of less than 0.05 mm and the spectral power of the signal was never greater than 0.0002 mm^2 Hz^{-1}. In the presence of ripples due to the breakers, the r.m.s. level is on the order of 1 mm and the peak spectral power is on the order of 0.1 mm^2 Hz^{-1}. Thus, the noise level was found to be sufficiently low for the measurements reported herein.

The data from each run were characterized by a high-frequency small-amplitude oscillatory signal superposed on a low-frequency oscillation caused by the starting transient during each run. This low-frequency oscillation was found by Duncan (1981) to have a period about equal to the period (as measured in the reference frame of the hydrofoil) of a wave with group velocity equal to the hydrofoil speed. For example, for $U_\infty = 80$ cm s^{-1}, the frequency of the transient in the frame of reference of the hydrofoil is about 0.5 Hz. This low-frequency oscillation, while probably not influencing the small ripples very much, can have a substantial effect on the r.m.s. amplitude of the surface height. Thus, it was decided to high-pass filter the data before processing. In most cases, a fast Fourier transform (FFT) of a sequence of 8192 data points from each run was obtained, the spectral amplitudes at frequencies below two times the frequency of the transient were then zeroed and the transform was inverted to yield the filtered signal. An example of the signal before and after filtering is shown in figure 4.

The next step in the data processing was to take an FFT of the data with 1024 points in 15 overlapping data sets. The overlapping data sets are recommended by Press *et al.* (1986) to increase the statistical significance of the resulting spectrum. However, this increased statistical significance is accompanied by a poorer frequency resolution in the spectrum, since the data record for each FFT is only 1024 points long.

2.4. *Hot-film anemometers*

Hot-film anemometers were used to measure the horizontal and vertical components of the mean and fluctuating velocity in the wake of the breaking waves. The hot-film anemometer system was manufactured by Thermo-Systems, Inc. and consisted of a model 1053B anemometer and three model 1 248A-10 miniature X-probes. An overheat ratio of 1.1 was used. The sensing elements of the X-probes consisted of a glass rod, plated with a thin platinum film approximately 0.1 μm thick. The sensor length was 1.25 mm with an effective sensing length of 0.51 mm in the centre due to gold plating extending from the sensor supports. The sensing length had a thin quartz coating of thickness 0.8 μm. The diameter of the coated sensing length was 0.025 mm. The data were acquired on a PC with a 12-bit digitizing board and a sampling rate of 1000 Hz.

Since the hot-film probes remain in the water between runs, there is a combination of electronic drift and fouling of the probes that changes the calibrations and is particularly damaging to the measurement of absolute velocity. These problems necessitate calibration of the probes before every run. Since both vertical and horizontal velocities are being measured, the probes must be calibrated by running at various angles of attack as well as various speeds. A sequence of tests was performed to minimize the number of runs needed for a good calibration and the wait time between runs in order to reduce drift of the probes to a minimum while allowing an adequate time for the residual disturbances in the tank to decay. The following scheme was determined to be optimum. First, the hydrofoil was disabled and the probe rake was tilted to $+10°$ angle of attack. It was then towed along the tank with five different towing speeds in a single run. Each towing speed was maintained for about 2 s during the run. Next, the carriage was returned to its starting position and the rake was tilted to an angle of attack of $-10°$. A waiting period of about ten minutes was allowed for the tank to settle. Then another towing run was made with five different speeds, the carriage was brought back to its starting position and the rake was returned to zero angle of attack. After 10 minutes, the run with the hydrofoil was made and the actual data were recorded. The probe rake was adjusted for each run so that the vertical position of each probe relative to the mean water level was the same in each calibration run and in the final data-taking runs.

Following the work of Wygnanski, Champagne & Marasli (1986) the X-probes were calibrated using the following equations:

$$u - A_{3j}v = P_j(E_j) \qquad (j = 1, 2), \tag{2.1}$$

where u and v are the horizontal and vertical velocity components, E_1 and E_2 are the bridge voltages from the two probe elements and P_1 and P_2 are polynomials given by

$$P_j(E_j) = \sum_{n=0}^{2} A_{nj} E_j^n. \tag{2.2}$$

The unknown constants A_{nj}, $n = 0, \ldots, 3$, were determined by least-squares fit. Correlation coefficients of the order of 0.9998 were typically obtained. The wait times and calibration method were tested by making a third run without the hydrofoil and with the rake tilted to a third angle of attack. It was found that the third run could be predicted accurately with the data from the first two runs and the above equation.

The final problem in the measurement of fluid velocity was the interaction of the hot-film X-probes with air bubbles entrained into the flow by the breaking waves. A set of experiments was performed to examine this problem. In these experiments,

U_∞ (cm s^{-1})	d (cm)	α (deg.)	θ_{br} (deg.)	h_{br} (cm)	H_{br} (cm)	A_{br} (cm^2)	D_T/D_0	L_θ (cm)
60	21.9	10	12.7	1.88	2.37	4.18	1.77	0.13
80	28.7	10	12.6	2.63	3.46	8.83	1.18	0.15
80	26.7	10	8.1	2.84	3.30	20.51	1.77	0.23
80	24.2	10	5.7	3.44	3.67	38.98	2.37	0.31
100	26.5	5	9.4	4.41	4.78	36.51	1.49	0.30

TABLE 1. Experimental conditions (U_∞ is the speed of the hydrofoil, d is the depth of submergence of its trailing edge, and α is its angle of attack) and geometrical characteristics of the mean shape of the breaking waves (see figure 1 for definitions of θ_{br}, h_{br}, H_{br} and A_{br}).

small air bubbles were introduced into the tank through the mouth of a tube placed about 30 cm below the water surface in the otherwise quiescent tank. The hot-film X-probe passed over the mouth of the tube at the time the bubble was rising and encountered the bubble. The results show that when the probe hits a bubble, the effect on the voltages of the hot-film probe is clearly discernible from velocity fluctuations in the turbulent wake and the probe recovers to its original calibration very quickly after encountering the bubble. From runs with the hydrofoil, it was found that typically at most one bubble encounters a given probe during each run. Thus, the voltage fluctuations from the bubble encounters were removed from the data and replaced with a linear interpolation between the data point just before the beginning of the encounter and the data point just after the encounter.

The processing of the records of u and v from each run was performed in the same manner as the surface height fluctuation records described in the previous subsection.

3. Results

3.1. *Experimental conditions*

A total of five combinations of U_∞, α, and d were chosen for the experiments, see table 1. These conditions included three combinations of U_∞ and α with one value of d at $U_\infty = 60$ cm s^{-1}, three values of d at $U_\infty = 80$ cm s^{-1}, and one value of d at $U_\infty = 100$ cm s^{-1}. The values of d for $U_\infty = 80$ cm s^{-1} were chosen so that the breaker was very weak at the largest value of d, and strong enough at the smallest value of d to make the residual wavetrain almost non-existent. The other depth of submergence at $U_\infty = 80$ cm s^{-1} and those at the other two speeds were chosen to produce breakers whose strengths were roughly in the middle of the range between the weakest breaker possible and the breaker with nearly no following wavetrain.

3.2. *Profiles of the breaking waves*

In this section, properties of the average and fluctuating components of the shape of the breaking waves are presented. Geometrical parameters measured from the average profiles are used in §4 to scale the measurements of fluctuating quantities in the breaking region and the wake. The breaking wave profiles were obtained from photographs as described in §2.2. About 25 profiles were obtained for each experimental condition. At each horizontal location in the profile, the mean surface height, $\bar{\eta}(x)$, and the r.m.s. fluctuation about the mean, η_{rms} (where $\eta_{rms} = (\overline{\eta'^2})^{1/2}$ and $\eta' = \eta - \bar{\eta}$), were then calculated. Figure 5 shows plots of $\bar{\eta}(x)$ and η_{rms} for the three experimental conditions with $U_\infty = 80$ cm s^{-1}. Similar plots for the other two experimental conditions are available but are not presented. For all five experimental

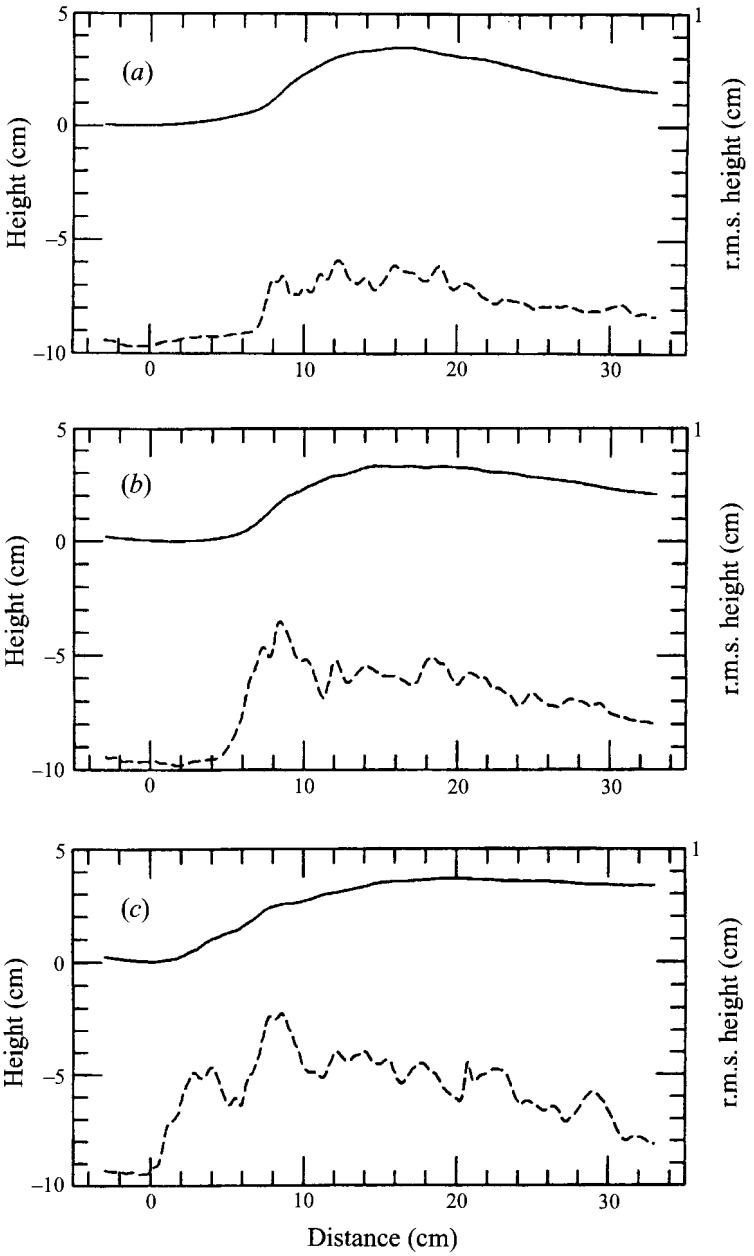

FIGURE 5. Profiles of three breaking waves with the same towing speed including the average profile (———) and the r.m.s. fluctuation about the average (– – – –). $U_\infty = 80$ cm s^{-1}, $\alpha = 10°$: (*a*) $d = 28.7$ cm; (*b*) $d = 26.7$ cm; and (*c*) $d = 24.2$ cm.

conditions, the profile in the trough ahead of the breaker was found to be nearly the same in every photograph. This is reflected in the relatively small values of η_{rms} in this region. As one moves downstream from the trough, η_{rms} begins to grow. At about the same horizontal location, the average profile shows a rapid change in slope. One can imagine the leading edge or 'toe' of the breaking region oscillating back and forth along the smooth wave profile. In the average profile, this appears as a nearly linear increase in height in the transition between the smooth surface ahead of the breaker

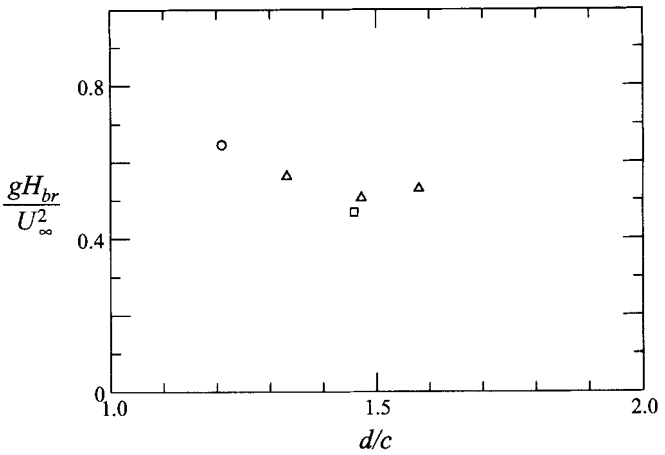

FIGURE 6. Breaker Froude number, $H_{br}g/U_\infty^2$, versus depth of submergence over the chord of the foil, d/c. See figure 1 for definitions. ○, $U_\infty = 60$ cm s^{-1}, $\alpha = 10°$; △, $U_\infty = 80$ cm s^{-1}, $\alpha = 10°$; and □, $U_\infty = 100$ cm s^{-1}, $\alpha = 5°$.

and the surface of the breaking region. Similar results are reported by Walker *et al.* (1996). In the following, the position of the toe in the average profile is taken as the horizontal position on the forward face where η_{rms} starts to rise from its value on the smooth water surface in the trough ahead of the breaker.

Several geometrical characteristics of the average profiles were measured. For some of these characteristics, it was necessary to define the lower boundary of the breaking region. This boundary was taken as a straight line that was approximately tangent to the free surface just upstream of the toe position and extended downstream to the point where the line intersected the wave profile. This intersection point was behind the crest in all cases. This straight line is shown schematically with several other geometrical characteristics of the breaking wave in figure 1. These geometrical characteristics include the wave height from the trough in front of the breaker to the crest of the breaking wave (H_{br}), the angle relative to the horizontal of the lower boundary of the breaking region (θ_{br}), the area of the breaking region (A_{br}) defined as the area between its lower boundary and the average water surface, and the height from the toe of the breaking region to the crest (h_{br}). These data are presented in table 1. It should be noted that in the work of Duncan (1981,1983*a*) the bottom of the breaking region and the geometrical characteristics defined above were measured for each frame in a sequence of photographs and then averaged to obtain the quantities listed in table 1. The present method using the average profiles was chosen for reliability with the computerized image analysis methods used herein.

From the data for $U_\infty = 80$ cm s^{-1} shown in table 1, it can be seen that h_{br} increases as d is decreased. At the smallest d, h_{br} is nearly equal to H_{br}. This indicates that for the strongest breakers, the toe of the breaking region is located nearly at the trough ahead of the breaker. In a previous study, Duncan (1981) found that the height and speed of the breaking wave were well correlated by the equation $gH_{br}/U_\infty^2 = 0.6$ with minimum and maximum individual values of the constant on the right-hand side equal to 0.57 and 0.64, respectively, where g is the gravitational acceleration. For the present data, a plot of the breaker height, $H_{br}g/U_\infty^2$, versus d/c, where c is the chord of the foil, is given in figure 6. The average, minimum and maximum values of $H_{br}g/U_\infty^2$ are 0.54, 0.47 and 0.65, respectively.

U_∞ (cm s^{-1})	d (cm)	α (deg.)	η_{br} (cm)	λ_{br} (cm)	η_{rms} (mm) T1	η_{rms} (mm) T2	f_w (Hz)
60	21.9	10	0.13	3.22	0.67		12.18
80	28.7	10	0.21	4.53	0.89	0.80	10.60
80	26.7	10	0.30	4.86	1.22	1.05	8.35
80	24.2	10	0.36	6.23	1.62	1.32	6.84
100	26.5	5	0.42	6.61	1.43	1.28	7.81

TABLE 2. Results describing the surface height fluctuations: average r.m.s. amplitude on the breaking region, η_{br}; average wavelength on the breaking region, λ_{br}; r.m.s. amplitude, η_{rms}, at the first and second trough of the following wavetrain (T1 and T2, respectively); and frequency of the spectral peak, f_w, for measurements in the following wavetrain.

The curvature of the average surface profiles just behind the crest in figure 5 is related to the amplitude, a_f, of the wavetrain following the breaker. Smaller curvatures indicate that the average surface behind the breaker is nearly flat, while larger curvatures indicate a substantial following wavetrain. From figure 5, it can be seen that this curvature decreases with d. This relationship between the breaker and the following wavetrain was first noted by Duncan (1981, 1983*a*), explained theoretically by Cointe & Tulin (1994), and was also noted by Walker *et al.* (1996).

Using measurements of the geometry of the breaker, and the mean velocity profile in the wake of the breaker, Duncan (1981, 1983*a*) found that the momentum deficit in the wake was equal to $0.52\rho g A_{br} \sin\theta_{br} \equiv D_T$ where ρ is the density of water. This is the downslope component of the weight of the breaking region, assuming that the density of the fluid in the breaking region is approximately equal to ρ. It was also pointed out by Duncan (1983*b*) that the maximum resistance, D_0, due to non-breaking waves on the hydrofoil was equal to $0.02\rho U_\infty^4/g$. The ratio D_T/D_0 is given in table 1 for the five conditions studied here. Note that in the three cases with $U_\infty = 80$ cm s^{-1}, the value increases from 1.18, where the breaker was observed to be about the weakest possible for the given towing speed, to 2.37, where the breaker was observed to be quite strong. Duncan (1983*a*) found D_T/D_0 to range from about 1 to 3 in general agreement with the present results. The three cases with intermediate breaker strengths ($U_\infty = 60$ cm s^{-1}, $d = 21.9$ cm; $U_\infty = 80$ cm s^{-1}, $d = 26.7$ cm; and $U_\infty = 100$ cm s^{-1}, $d = 26.5$ cm) have values of D_T/D_0 near 1.68.

Two parameters describing the fluctuations in surface height on the breaking region were computed as well: the average value of η_{rms}, η_{br}, and the average wavelength of the fluctuations, λ_{br}. In computing η_{br}, data like those shown in figure 5 were averaged over the profile of the breaker from the toe to the crest. The wavelength was computed by first counting the number of times the instantaneous profiles crossed the average profile in each image. Then the average number of crossings was divided into the length of the line from the toe to the crest and multiplied by two. This length was then averaged over the number of images for each experimental condition to yield λ_{br}. As can be seen from table 2, for $U_\infty = 80$ cm s^{-1}, both η_{br} and λ_{br} increase with decreasing d while for the three intermediate-strength breakers both η_{br} and λ_{br} increase with U_∞. The behaviour of η_{br} for $U_\infty = 80$ cm s^{-1} is qualitatively similar to that reported by Walker *et al.* (1996, figures 3, 4, and 5) for $U_\infty = 108$ cm s^{-1}.

3.3. *Measurements of the ripples in the wake*

The ripples in the wake of the breaking wave were measured with the wave-height gauge on the moving instrument carriage as described in §2.3. For each experimental

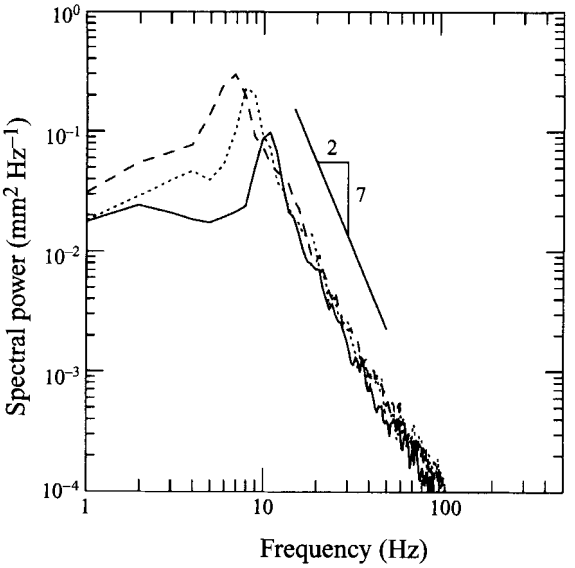

FIGURE 7. Spectra of the surface height fluctuations, η', at the second trough of the residual wavetrain behind three breaking waves. $U_\infty = 80$ cm s^{-1}, $\alpha = 10°$. ———, $d = 28.7$ cm; ·····, $d = 26.7$ cm; and – – – –, $d = 24.2$ cm.

condition and probe location, three to six runs were made and the r.m.s. and spectral data were averaged over these runs. Measurements were taken at the crests and troughs in the following wavetrain for up to three wavelengths behind the breaker for the experimental conditions with $U_\infty = 80$ cm s^{-1}, at the first trough behind the breaker for the case with $U_\infty = 60$ cm s^{-1}, and at the first and second trough for the case with $U_\infty = 100$ cm s^{-1}.

Log-log plots of spectral power of the ripples versus frequency for data from the second trough after the breaker for the three cases with $U_\infty = 80$ cm s^{-1} are shown in figure 7. All the spectra are sharply peaked. The frequency of the spectral peak decreases and the spectral level increases as the breaker becomes more intense (i.e. smaller d). The shapes of the spectra are quite similar and at high enough frequencies the spectra are nearly the same straight line on the log-log plot. Thus, it appears that the high-frequency portion of the spectrum is saturated in some sense. The straight line drawn to the right of the spectra has a slope very close to that of the high-frequency part of the spectra. This line represents a power law with frequency to $-7/2$.

Five spectra from data taken at the troughs and crests of the following wavetrain for the experimental condition $U_\infty = 80$ cm s^{-1}, $\alpha = 10°$ and $d = 28.7$ cm are shown in figure 8. This is the weakest breaker at $U_\infty = 80$ cm s^{-1}. The shapes of the spectra are quite similar as is the frequency of the spectral peak. However, the overall amplitude of the spectra varies from one downstream location to the next. Data from the other experimental conditions exhibited similar behaviour. To show the behaviour of the overall amplitude of the spectrum as a function of distance downstream, a plot of η_{rms} versus distance downstream, x/λ_0, where $\lambda_0 = 2\pi U_\infty^2/g$, is given in figure 9. The points at $x/\lambda_0 = 0$ are values of η_{br} from table 1. The overall level of η_{rms} increases with decreasing d. For the case with $d = 28.7$ cm, the steepness of the following wavetrain is fairly high, $a_f k_0 = 0.12$ (where $k_0 = 2\pi/\lambda_0$), and η_{rms} shows an oscillation with x/λ_0 such that there are higher values at the crests and lower values at the

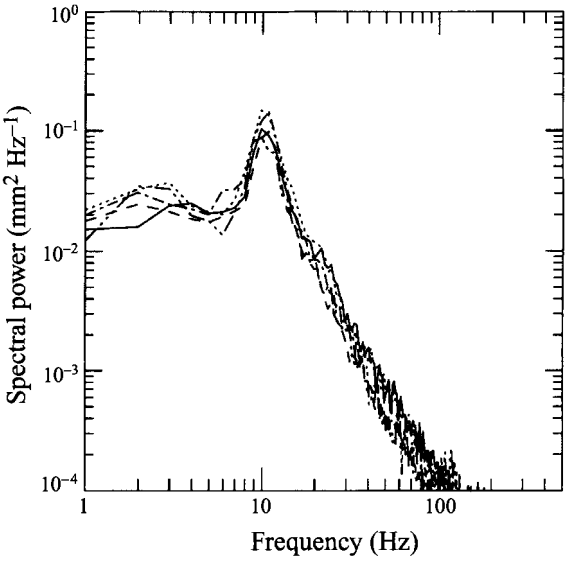

FIGURE 8. Spectra of the surface height fluctuations, η', at the crests and troughs of the residual wavetrain behind the breaking wave. $U_\infty = 80$ cm s^{-1}, $\alpha = 10°$, $d = 28.7$ cm. ———, first trough; · · · · · · · ·, first crest; – – – –, second trough; – · – · –, second crest; – · · – · · – · · –, third trough.

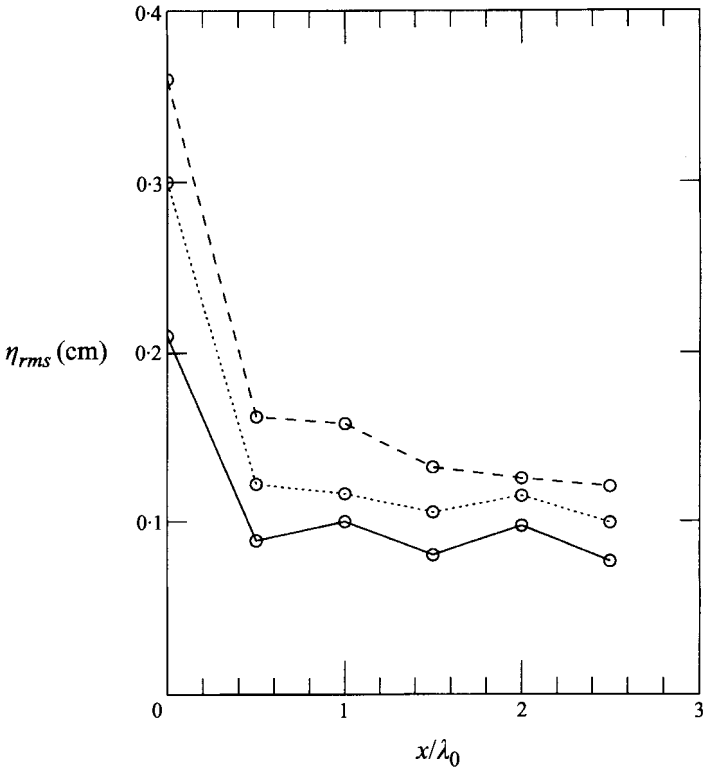

FIGURE 9. Root-mean-square surface height fluctuation versus distance behind the breaker. $U_\infty = 80$ cm s^{-1}, $\alpha = 10°$. $x/\lambda_0 = 0.5$ is the first trough after the breaker, $x/\lambda_0 = 1.0$ is the first crest after the breaker, etc. $\lambda_0 = 2\pi U_\infty^2/g$ is the wavelength of the following wave. ———, $d = 28.7$ cm, $a_f k_0 = 0.12$; · · · · · · · ·, $d = 26.7$ cm, $a_f k_0 = 0.06$; – – – –, $d = 24.2$ cm, $a_f k_0 = 0.03$.

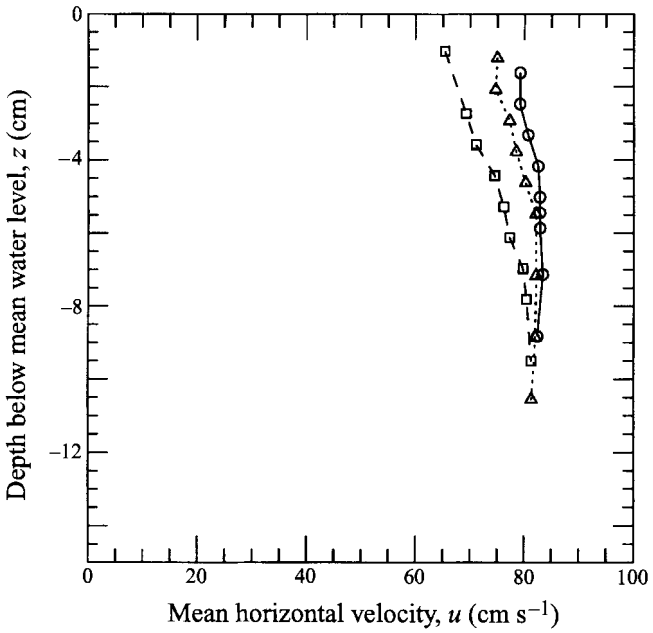

FIGURE 10. Average horizontal velocity versus depth at the second trough of the following wavetrain for $U_\infty = 80$ cm s^{-1}, $\alpha = 10°$: ———, $d = 28.7$ cm; · · · · · · · , $d = 26.7$ cm; and – – – –, $d = 24.2$ cm.

troughs. This oscillation is in qualitative agreement with the theory of the interaction of short and long waves as given by Longuet-Higgins & Stewart (1960) though the theory was derived for potential flow. As the depth of submergence is decreased, the oscillation in the data decreases as does the steepness of the following wavetrain ($a_f k_0 = 0.06$ for $d = 26.7$ cm and $a_f k_0 = 0.03$ for $d = 24.2$ cm). Plots of η_{rms} versus x/λ_0 for the conditions with $U_\infty = 60$ and 100 cm s^{-1} are not presented, since the data were not taken at all values of x/λ_0.

In order to summarize the above-described data, the values of η_{rms} at the first and second troughs of the following wavetrain and the frequency of the spectral peak, f_w, are given in table 2 for all five experimental conditions. Note that the values of η_{rms} for the cases with $U_\infty = 80$ cm s^{-1} increase with decreasing d, and that for the three intermediate breaker strengths, the values increase with increasing U_∞. The values of f_w show the opposite behaviour.

3.4. *Velocity measurements*

The velocity measurements taken at the second trough after the breaking wave are presented in this subsection. The mean velocity is presented first. The mean horizontal velocity, $u(z)$, for the three cases with $U_\infty = 80$ cm s^{-1} is shown in figure 10. The profiles are quite similar to those reported by Battjes & Sakai (1981) and Duncan (1981, 1983*a*). Far from the free surface, the velocity is nearly equal to the towing speed (80 cm s^{-1}). From this depth, the velocity first increases (for the weakest breaker) and then decreases as the surface is approached from below. The increase is due to the flow field of the following wavetrain, and is most pronounced for the case with $d = 28.7$ cm where the following wavetrain is largest. For the case with $d = 24.2$ cm, the amplitude of the following wavetrain is nearly zero, and the increase in the velocity at intermediate depths is also negligible. The velocity at the topmost point

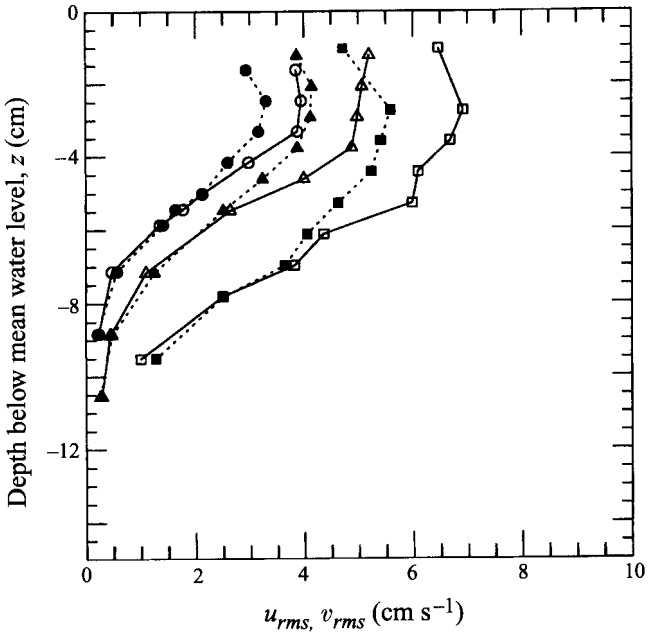

FIGURE 11. Plots of u_{rms} (open plotting symbols) and v_{rms} (closed plotting symbols) versus depth at the second trough of the following wavetrain for $U_\infty = 80$ cm s^{-1}, $\alpha = 10°$: ○, $d = 28.7$ cm; △, $d = 26.7$ cm; and □, $d = 24.2$ cm.

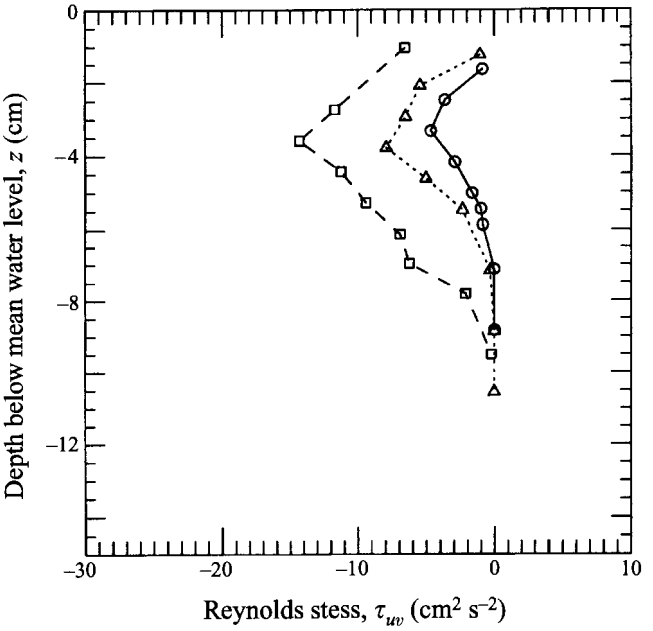

FIGURE 12. Reynolds stress, τ_{uv}, versus depth at the second trough of the following wavetrain for $U_\infty = 80$ cm s^{-1}, $\alpha = 10°$: ○, $d = 28.7$ cm; △, $d = 26.7$ cm; and □, $d = 24.2$ cm.

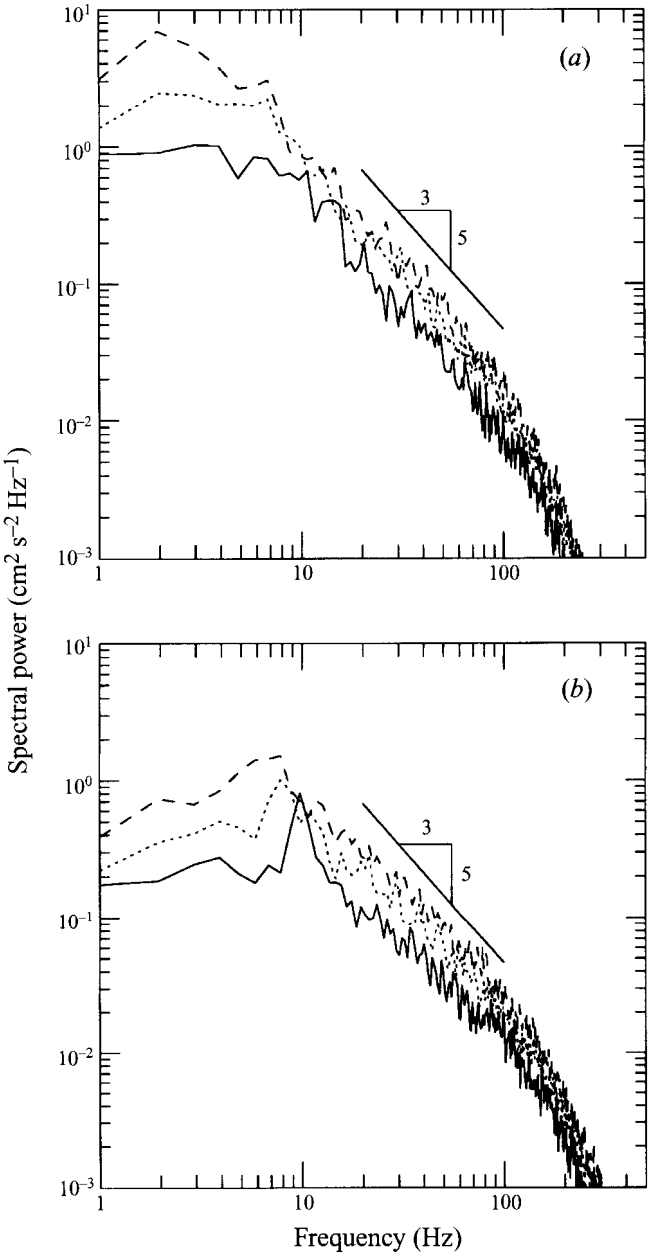

FIGURE 13. Spectra of u' (*a*) and v' (*b*) for the measurement depth closest to the free surface at the second trough of the following wavetrain. $U_\infty = 80$ cm s^{-1}, $\alpha = 10°$: ———, $d = 28.7$ cm; · · · · · · · ·, $d = 26.7$ cm; and – – – –, $d = 24.2$ cm.

decreases and the thickness of the region with $u \leqslant U_\infty$ increases as d is decreased. Though the data are qualitatively reasonable, it is not possible to use them to get the integrated momentum deficit of the wake because of the probe drift problems mentioned above, and the fact that it is the difference between the plotted data and the velocity in the flow field of a potential flow wave with the same amplitude and phase speed as the following wavetrain that must be integrated to get the drag due

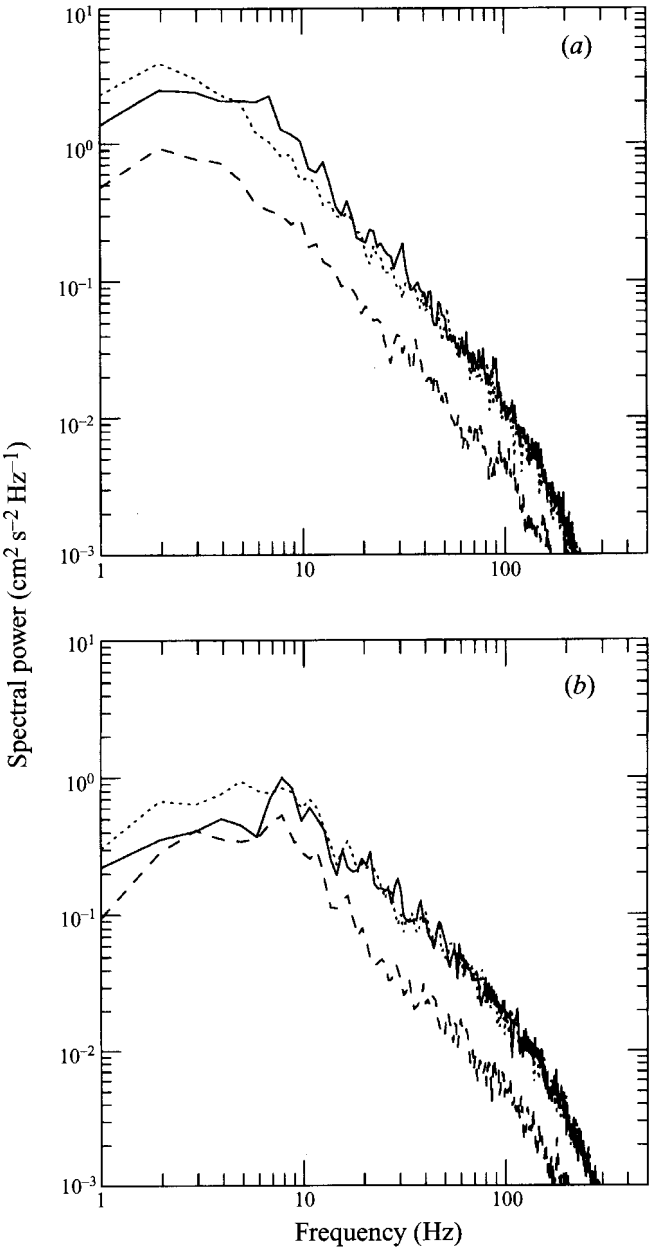

FIGURE 14. Spectra of u' (*a*) and v' (*b*) for various measurement depths (z) at the second trough of the following wavetrain. $U_\infty = 80$ cm s^{-1}, $\alpha = 10°$, $d = 26.7$ cm: ———, $z = -1.2$ cm; ·····, $z = -2.9$ cm; and – – – –, $z = -5.5$ cm.

to breaking. This difference is on the order of 10% of $u(z)$ and therefore is quite sensitive to the errors in the measured values of $u(z)$.

Distributions of $(\overline{u'^2})^{1/2} \equiv u_{rms}$ and $(\overline{v'^2})^{1/2} \equiv v_{rms}$ at the second trough behind the breaker are shown in figure 11 for the three cases with $U_\infty = 80$ cm s^{-1}. In all three cases, the intensities are quite small at the larger depths. These values begin to increase as the surface is approached. At first, u_{rms} and v_{rms} are nearly equal, but

closer to the surface u_{rms} is always greater than v_{rms}. The distributions of v_{rms} reach maxima at a depth of about 3 cm, and then decrease as the surface is approached. In contrast, the distributions of u_{rms} seem to be more or less constant as the surface is approached.

Distributions of the Reynolds stress, $-\overline{u'v'} \equiv \tau_{uv}$, in the wakes of the three breakers with $U_\infty = 80$ cm s^{-1} are given in figure 12. The values of τ_{uv} are all negative, while each distribution has a minimum value below the free surface and tends to zero at both the free surface and large depths. This behaviour is typical of Reynolds stress distributions in two-dimensional wakes. The magnitude of τ_{uv} increases with decreasing d.

Plots of the spectra of u' and v' for the measurement point closest to the surface for the three cases with $U_\infty = 80$ cm s^{-1} are shown in figure 13. The high-frequency parts of the spectra are quite similar while the low-frequency parts are not. At low frequencies, the u' spectra either level off or reach a broad peak at very low frequency while the v' spectra reach a peak at frequencies near 10 Hz. The frequencies of these peaks decrease with increasing breaker strength (decreasing d), and are about equal to the frequencies of the maxima in the spectra of η'. In the frequency range from 20 to 100 Hz, the spectra nearly follow a frequency to the $-5/3$ power law. In both the u' and v' spectra, the overall level of the spectra increases with increasing breaker intensity. The spectra of u' and v' at various measurement depths for $U_\infty = 80$ cm s^{-1} and $d = 26.7$ cm are shown in figure 14. The shape of the spectra of u' are fairly independent of measuring depth, while the v' spectra have a sharper peak close to the surface and broader peaks at deeper measuring depths.

4. Discussion

In this section, the relationships between the properties of the mean and fluctuating breaker shape and the ripples and turbulence in the wake are explored.

4.1. *Ripple generation and propagation*

We begin with the frequency–wavenumber characteristics of the ripples. It was noted in the previous section that the peak frequency, f_w, of the free-surface elevation spectra in the wake is nearly independent of x for each breaker (see figure 8). Walker *et al.* (1996) found this frequency to be constant throughout the wake and most of the breaking region, although in their measurements the frequencies were not well resolved due to a low temporal sampling rate. They also found that the wavenumber of the ripples decreased with distance downstream. It has been established experimentally by Battjes & Sakai (1981) and Duncan (1981, 1983*a*) that the turbulent wake of the breaker behaves like the half-wake of a two-dimensional body with the symmetry plane taken as the free surface. It has also been assumed in previous theoretical studies (Cointe & Tulin 1994) and shown experimentally (Lin & Rockwell 1994, 1996) that the breaking region is almost stagnant relative to the wave crest and rides over a fast-moving downstream flow. Thus, the flow in both the breaking region and the wake can be modelled as a spatially evolving free-surface shear flow, called the breaker shear flow hereafter. In this model, typical mean velocity profiles in the breaker shear flow (see figure 15) have the characteristic shape (with an inflection point) of mean velocity profiles in the wake of floating towed bodies. With this model in mind, it is shown in the following from the present measurements and linear stability analysis of the breaker shear flow that the ripples in the wake are primarily generated at the breaker.

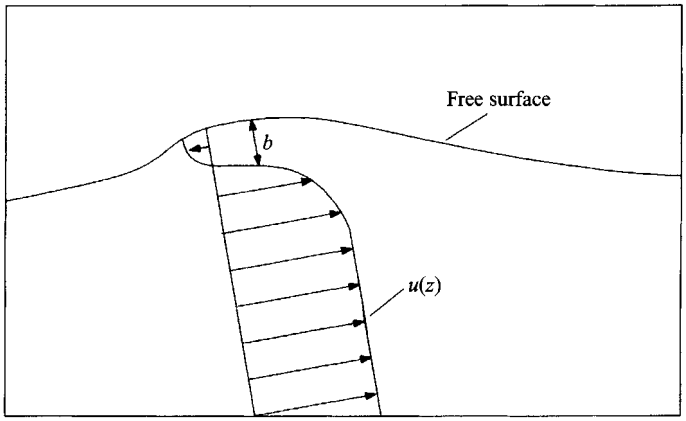

FIGURE 15. Schematic showing shear flow near the free surface in the breaking wave.

The formulation for the linear stability analysis of the breaker shear flow used herein is the one first presented in Triantafyllou & Dimas (1989), where it was established that parallel free-surface shear flows with mean velocity profiles $u(z)$ typical of our breaker shear flow are linearly unstable to certain disturbances. For completeness, the model and the basic instability physics of these flows are briefly described below. In linear stability analysis, a small two-dimensional disturbance flow is superimposed on the initial mean flow $u(z)$. All velocities are non-dimensionalized with respect to the free-stream velocity, U_∞, and all lengths with respect to the wake half-thickness, b, defined as the depth at which the mean velocity deficit, $U_\infty - u(-b)$, is half the total mean velocity deficit, $U_\infty - u(0)$. Then, the non-dimensional mean velocity profile becomes $U(Z) = U(z/b) = u(z)/U_\infty$.

The evolution of the unsteady disturbance flow is studied by linearizing the equations of motion with respect to the mean flow. Because the mean flow $U(Z)$ is parallel, wavy perturbations can be considered in the form

$$\Psi(X,Z,T) = \Phi(Z)\exp(\mathrm{i}(kX - \omega T)) \tag{4.1}$$

where $\Psi(X,Z,T)$ is the stream function of the disturbance flow, $\Phi(Z)$ is the eigenfunction, k is the wavenumber, ω is the frequency, X is the non-dimensional coordinate along the streamwise direction and T is the non-dimensional time. Then, the dispersion relation is obtained as an eigenvalue problem for the frequency ω, consisting of Rayleigh's equation:

$$\left(U - \frac{\omega}{k}\right)\left(\frac{\mathrm{d}^2\Phi}{\mathrm{d}Z^2} - k^2\Phi\right) - \frac{\mathrm{d}^2U}{\mathrm{d}Z^2}\Phi = 0 \tag{4.2}$$

subject to the linearized kinematic and dynamic free-surface boundary conditions, respectively:

$$\Phi(0) = \left(\frac{\omega}{k} - U(0)\right)a, \tag{4.3}$$

$$\left(\frac{\omega}{k} - U(0)\right)\frac{\mathrm{d}\Phi}{\mathrm{d}Z}(0) = \frac{a}{Fr^2}\frac{b}{L_\theta}, \tag{4.4}$$

and the condition that $\Phi \to 0$ as $Z \to -\infty$. In the above equations, a is the amplitude of the free-surface elevation, η, defined as

$$\eta(X,T) = a\exp(\mathrm{i}(kX - \omega T)), \tag{4.5}$$

L_θ is the momentum thickness of the mean flow, defined as

$$\frac{L_\theta}{b} = \int_{-\infty}^{0} U(1-U)\mathrm{d}Z, \tag{4.6}$$

and Fr is the Froude number of the flow, defined as

$$Fr = \frac{U_\infty}{(gL_\theta)^{1/2}}, \tag{4.7}$$

where g is the acceleration due to gravity. Therefore, the only non-dimensional parameter to control the behaviour of the inviscid instability is the Froude number.

The problem is transformed into a generalized algebraic eigenvalue problem, using a three-point centred finite-difference scheme for the spatial approximation, which is then solved numerically using a standard $Q-Z$ algorithm (Moler & Stewart 1973). A detailed description of the numerical method and discussion of the results is given by Triantafyllou & Dimas (1989), but the main results, considering our breaker shear flow, can be summarized as follows. The instabilities of such shear flows present two frequency (or wavenumber) ranges of unstable waves for each Froude number: one at low frequencies, called Branch I, and one at high frequencies, called Branch II. As the Froude number increases, the growth rates and the frequency range of the Branch I instability decrease. On the other hand, the growth rates of the Branch II instability increase, while the frequency range broadens and moves to lower frequencies. For low Froude numbers, the Branch I instabilities have larger growth rates and dominate, while for medium and high Froude numbers, the Branch II instabilities have larger growth rates and dominate. In both cases, as the Froude number increases, the frequency of the instability with the maximum growth rate decreases. Finally, the instability is convective for both branches with the exception of very high Froude numbers where the Branch II instability becomes absolute.

To establish that the ripples measured in the wake are generated by the instability of the shear flow at the breaker and are convected downstream, first we have to exclude the scenario of generation at downstream locations. This can be accomplished by computing the stability characteristics of the mean velocity profile of the strong breaker with $U_\infty = 80$ cm s^{-1} at the location of the second trough downstream of the breaker. The experimental measurements of the mean velocity profile are fitted with the curve

$$u(z) = U_\infty \left(1 - (1 - U(0)) \left(1 - \tanh\left(\sigma \left(\frac{z}{b}\right)^2\right)\right)\right) \tag{4.8}$$

where U_∞ is the free-stream velocity and $U(0)$ is the non-dimensional centreline velocity. The values $U_\infty = 80$ cm s^{-1}, $b = 3.9$ cm, $U(0) = 0.815$, $\sigma = 0.5493$ are used, and the corresponding profile is shown in figure 16. The stability analysis of this profile at $Fr = 3.2$ reveals that its Branch I instability has frequency $f = 2$ Hz and wavelength 36 cm for the most unstable disturbance, and its Branch II instability has frequency $f = 54$ Hz and wavelength 1.4 cm for the most unstable disturbance. Neither of these results agrees with the measured frequency $f = 6.84$ Hz at this location.

It is expected, therefore, that the disturbances are generated upstream at the breaker region where the mean velocity profile of the breaker shear flow has larger velocity deficit and smaller wake half-thickness, b. Since the instabilities of such a shear flow have a convective character and larger growth rates than the instabilities of velocity profiles downstream, they are expected to dominate the whole wake. The problem with

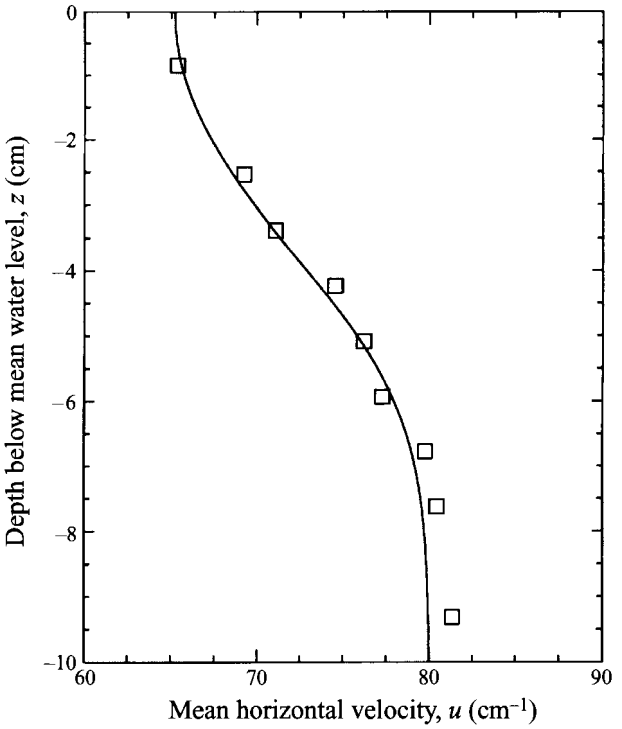

FIGURE 16. Distribution of $u(z)$ (data points) and curve fit for linear stability analysis at the second trough of the following wavetrain for $U_\infty = 80$ cm s^{-1}, $\alpha = 10°$, $d = 24.2$ cm.

the present data, though, is that it was difficult to obtain mean velocity measurements at the location of the breaker, therefore we cannot perform a stability analysis of a directly measured velocity profile. Instead, we consider the stability analysis of the theoretical velocity profile (4.8) for several values of the velocity deficit. It is theorized that the breaking region is a thin shear layer of nearly stagnant fluid containing on average a low-speed roller such that the flow is moving slowly upstream at the free surface. In consideration of this model, several values of the mean velocity deficit at the free surface ranging from 100% to 110% of U_∞ were considered. Using these velocity profiles, the frequency f of the most unstable disturbance for different Froude numbers is evaluated. For each velocity deficit, the plot of the Strouhal number

$$St = \frac{fL_\theta}{U_\infty} \tag{4.9}$$

with respect to the Froude number is shown in figure 17. As the velocity deficit increases, the curves move to lower values of the Strouhal number. For the Froude numbers considered, Branch II instabilities dominate over Branch I instabilities. On the same plot, the corresponding data from the measured frequencies are also shown where we have computed the momentum thickness of the wake, $L_\theta = D_T/U_\infty^2$, from the measurements of the shape of the breaking wave and the correlation of Duncan (1981, 1983*a*). The values of L_θ are given in table 1. Based on the stability analysis of the velocity profiles at appropriate Strouhal and Froude numbers obtained from figure 17, we can also compute the wavelengths of the instabilities corresponding to the five experimental conditions. A plot of these wavelengths together with the experimentally measured wavelengths at the breaker (λ_{br}) is shown in figure 18. Considering the

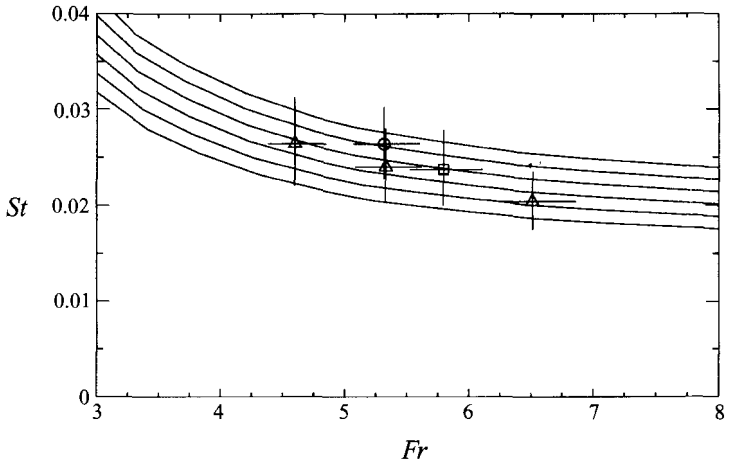

FIGURE 17. Strouhal number versus Froude number for ripple generation at the breaking region. The calculations with the linear stability model are represented by lines of constant mean velocity, $u(0)$, at the free surface. The top line is $u(0) = 0$ and the increment is $u(0) = -0.02U_\infty$. The symbols are the experimental data: ○, $U_\infty = 60$ cm s^{-1}; △, $U_\infty = 80$ cm s^{-1}; and □, $U_\infty = 100$ cm s^{-1}. The straight lines through each open data point are experimental error bars.

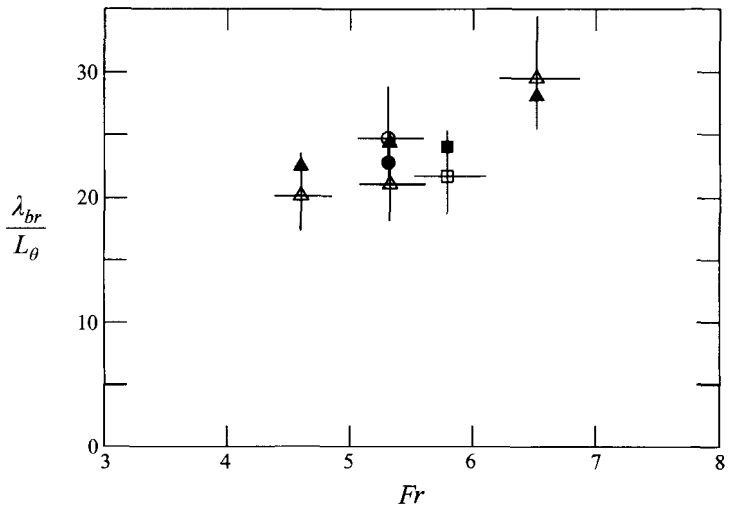

FIGURE 18. Plot of λ_{br}/L_θ versus Froude number. Open symbols are the experimental data. Filled symbols are the results of linear stability analysis: ○, $U_\infty = 60$ cm s^{-1}; △, $U_\infty = 80$ cm s^{-1}; and □, $U_\infty = 100$ cm s^{-1}. The straight lines through each open data point are experimental error bars.

experimental uncertainty, the agreement of the experimental data and the calculations shows that the ripples generated by the breaker are due to a Branch II instability of a velocity profile with a velocity deficit of about 105% of the free-stream velocity. Thus, the physical picture of the breaking region as a weak roller on the forward face of the wave seems to be consistent with the present data.

In addition to the above described linear calculations, the nonlinear evolution of the instabilities corresponding to the three breakers with $U_\infty = 80$ cm s^{-1} was also considered. At $t = 0$, a disturbance flow, which has the same wavenumber as the corresponding instability, is added to the mean velocity profile $u(z)$ and the nonlinear

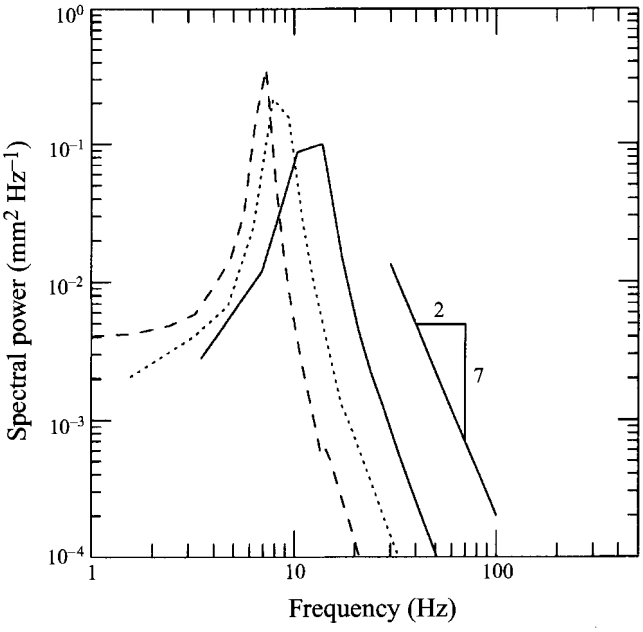

FIGURE 19. Spectra of surface height versus frequency from nonlinear stability calculations. $U_\infty = 80$ cm s^{-1}, $\alpha = 10°$. ———, $d = 28.7$ cm; · · · · · · · , $d = 26.7$ cm; and – – – –, $d = 24.2$ cm.

evolution of the flow is followed by a numerical simulation. The numerical simulation is based on the numerical solution of the Euler equations using spectral methods for the spatial discretization and an operator splitting scheme for the temporal discretization. Along the vertical direction, z, Chebyshev polynomials are used for the discretization, while the exact nonlinear free-surface boundary conditions are applied at the exact position of the free-surface using boundary-fitted coordinates. In the streamwise direction, periodic boundary conditions are applied, and Fourier modes are used for the discretization. Further details of the methodology are given by Dimas & Triantafyllou (1994). The computations for the present study were performed using 64 × 64 modes with a non-dimensional time step of 0.00025.

The free-surface elevation power spectra of these simulations are shown in figure 19. The sampling frequency was 1 KHz to coincide with the measurements. It is shown that, even after the nonlinear saturation of the instability, the peak frequencies of the ripples coincide with the linear analysis predictions. In the inertial range, the computed spectra do not follow a frequency to the $-7/2$ power law as do the experimental data in figure 7, probably because the simulations are two-dimensional.

As shown in figure 9, there is a sudden and significant drop of η_{rms} between the breaker and the crest of the following wave, while further downstream the drop is smaller. As we have established so far, the ripples are generated at the breaker and propagate downstream over the breaker shear flow. Their apparent frequency remains constant, therefore their wavenumber should change with respect to the downstream location due to the spatial variation of the mean velocity profile in the streamwise direction.

It can be assumed that far from the breaker, the mean flow behaves like the mean flow of the far half-wake behind a two-dimensional body in a uniform unbounded

stream. This means that the maximum velocity deficit decreases like

$$U_\infty - U_o \sim x^{-1/2} \tag{4.10}$$

where U_o is the mean velocity at $z = 0$, which corresponds to the average free-surface position. It can also be assumed that far from the breaker, the interaction of the ripples with the wake mean flow behaves similarly to the propagation of linear waves in deep water over a spatially varying current with velocity U_o. Considering the effect of both gravity and capillarity, the dispersion relation is

$$\omega_0 = \omega - kU_o = (gk + \gamma k^3)^{1/2} \tag{4.11}$$

where ω_0 is the frequency relative to still water, the apparent frequency, ω, remains constant, and γ is the ratio of surface tension to density. Therefore, as we move downstream and U_o increases, the wavenumber decreases. Using (4.10) for the behaviour of U_o, it can be easily shown from (4.11) that the wavenumber deficit decreases like

$$k - k_\infty \sim x^{-1/2} \tag{4.12}$$

where k_∞ is the wavenumber as $x \to \infty$ and $U_o \to U_\infty$.

In order to explain the behaviour of η_{rms} in the wake of the breaker, the conservation of wave action principle is considered. This principle implies that the wave action flux B of the ripples remains constant along the wake and equal to its value at the breaker where the ripples are generated. Based on linear wave theory in deep water (Peregrine 1976), the wave action flux B is defined as

$$B = E\frac{c_g + U_o}{\omega - kU_o} = \frac{1}{2}\rho\,(g + \gamma k^2)\,a^2\frac{c_g + U_o}{\omega - kU_o} \tag{4.13}$$

where E is the wave energy density, $c_g (= \partial\omega_0/\partial k)$ is the wave group velocity, and a is the wave amplitude. Then, far from the breaker, using (4.10) for the behaviour of U_o and (4.12) for the behaviour of k, it can be easily shown from the conservation of wave action flux (4.13) that the wave amplitude deficit decreases like

$$a - a_\infty \sim x^{-1/2} \tag{4.14}$$

where a_∞ is the wave amplitude as $x \to \infty$. Therefore, in the far wake, it is expected that η_{rms} will decrease like $x^{-1/2}$. This is shown in figure 20 where $(U_\infty^2/(g\eta_{rms}))^2$ is plotted with respect to x/λ_0. The solid straight lines shown in the figure are from a least-squares fit to the three points from the troughs of the following wave in each data set. It can be seen that each line is a good fit to the data. Similar fitting of the data at the crests is not meaningful since there are only two data points for each wave. It should be noted that the above wave action analysis (4.13) cannot be used to predict the behaviour of η_{rms} near the breaker because in this region the frequencies and wavenumbers (see figures 17 and 18) do not follow the dispersion relation (4.11).

4.2. *Turbulence and ripples in the wake*

In this subsection, the velocity fluctuations and their relationship with the surface ripples in the wake are discussed. We begin by comparing the velocity fluctuations to other published results including the study of breaking waves by Battjes & Sakai (1981), several studies of the wakes of two-dimensional bodies in an infinite fluid and studies of free-surface turbulence. Battjes & Sakai (1981) reported measurements of the vertical distributions of u_{rms} and τ_{uv} at a number of streamwise locations in two breaking waves. The present distributions of u_{rms} (figure

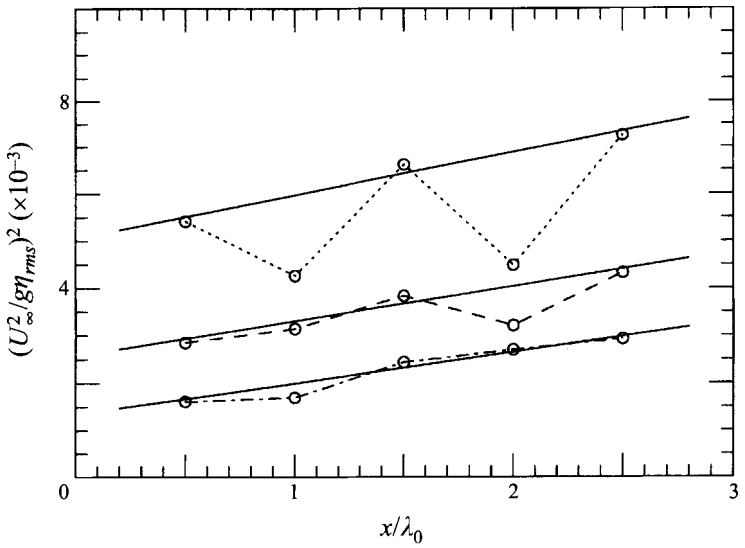

FIGURE 20. Plot of $(U_\infty^2/(g\eta_{rms}))^2$ versus x/λ_0 for $U_\infty = 80$ cm s^{-1}. The first trough after the breaker is $x/\lambda_0 = 0.5$; the first crest after the breaker is $x/\lambda_0 = 1.0$; etc. where $\lambda_0 = 2\pi U_\infty^2/g$. ·····, $d = 28.7$ cm, $a_f k_0 = 0.12$; – – – –, $d = 26.7$ cm, $a_f k_0 = 0.06$; – · – · –, $d = 24.2$ cm, $a_f k_0 = 0.03$.

11) and τ_{uv} (figure 12) are qualitatively similar to figures 3 (u_{rms}) and 4 (τ_{uv}) of Battjes & Sakai (1981). Unfortunately, no information on the breaker (other than the flow speed) was reported in their paper so a quantitative comparison with the present results is difficult.

The comparison with two-dimensional wake flows yields a number of interesting results. In the present measurements, $u_{rms} \geqslant v_{rms}$, v_{rms} and τ_{uv} reach a maximum below the free surface, and u_{rms} stays near its maximum for two or three measurement points just below the free surface for each wave. Some aspects of this behaviour are found in two-dimensional wakes in unbounded flows at similar values of x/θ (where θ is the momentum thickness). Chevray & Kovasznay (1969) reported one such set of measurements for the wake of a thin flat plate. They presented distributions of u_{rms}, v_{rms} and τ_{uv} for x/θ locations ranging from 0 (the trailing edge) to 414. In the present study, using the computed values of momentum thickness, L_θ, and taking the streamwise measurement position in the second trough of the following wavetrain to be at $x = 1.5\lambda_0$ for each case, the resulting values of $x/2L_\theta$ ($\approx x/\theta$) range from 99 to 205 (see table 3). Thus, the present results can be compared to the results of Chevray & Kovasznay that were taken at $x/\theta = 86$ and 258. In both the flat-plate data and the present data, $u_{rms}/v_{rms} > 1$; however, at equivalent x/θ the ratios of the maximum values, U_{rms}/V_{rms} (where U_{rms} and V_{rms} are the maximum values of u_{rms} and v_{rms}, respectively, at a given x), are not the same in the two flows. For example, $U_{rms}/V_{rms} \approx 1.6$ at $x/\theta = 86$ for Chevray & Kovasznay while for the present data it is 1.2 at $x/2L_\theta = 98$. Another difference between the two flows is that in the flat-plate wake the shapes of the u_{rms} and v_{rms} distributions are quite similar with peak values off the wake axis and a local minimum on the wake centreline. In the present data, v_{rms} reaches a maximum away from the free surface and u_{rms} is more or less constant as the free surface is approached. A decrease in v_{rms} and an increase in u_{rms} as the free surface is approached in a turbulent flow has been observed in two-dimensional open channel flows (Komori *et al.* 1982; Rashidi & Banerjee 1988), in a two-dimensional

U_∞ (cm s^{-2})	d (cm)	x/L_θ	U_{rms} (cm s^{-1})	V_{rms} (cm s^{-1})	Re_c	$\eta_{rms}g/(U_\infty V_{rms})$
60	21.9	266			2800	
80	28.7	410	4.0	3.3	4400	0.297
80	26.7	267	5.2	4.2	6700	0.307
80	24.2	198	6.9	5.6	9000	0.289
100	26.5	320	5.7	4.6	11000	0.273

TABLE 3. Results describing U_{rms} ($\equiv \max\{u_{rms}\}$) and V_{rms} ($\equiv \max\{v_{rms}\}$) at the second trough of the following wavetrain and their relationship with η_{rms} at the same location.

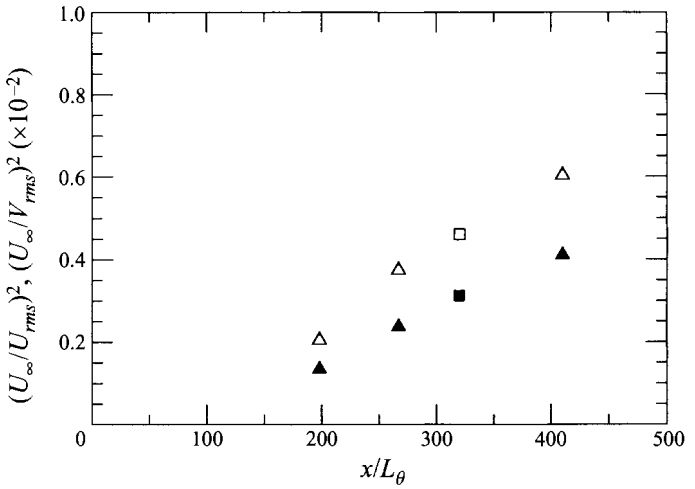

FIGURE 21. Plot of $(U_\infty/U_{rms})^2$ (filled symbols) and $(U_\infty/V_{rms})^2$ (open symbols) at the second trough of the following wavetrain versus x/L_θ. △, $U_\infty = 80$ cm s^{-1}; and □, $U_\infty = 100$ cm s^{-1}.

free-surface jet (Swean *et al.* 1989) and in a three-dimensional jet beneath a free surface (Anthony & Willmarth 1992).

A summary plot of $(U_\infty/u_{rms})^2$ on the wake centreline versus $x/2\theta$ from published studies of wakes generated by circular cylinders is presented in figure 2 of Wygnanski *et al.* (1986). For each experiment, defined by a particular Reynolds number and cylinder aspect ratio, the data follow a straight line. However, each data set follows a different straight line. Further, Wygnanski *et al.* (1986) measured flows behind airfoils, cylinders and screens, and attributed the differences in the curves of, for instance, $(U_\infty/u_{rms})^2$ versus $x/2\theta$ to the initial conditions in each wake and the influence of these initial conditions on the wake stability. In figure 21 of the present paper, a plot of the minimum values of $(U_\infty/u_{rms})^2$ and $(U_\infty/v_{rms})^2$ versus x/L_θ is presented. It should be noted that, unlike the data sets in typical studies of wakes behind two-dimensional bodies, which plot data for a single Reynolds number and various values of x, each of the present data points correspond to a separate Reynolds number and x/L_θ pair. For instance, the three data points for the cases with $U_\infty = 80$ cm s^{-1} are equivalent to measurements with cylinders of three different diameters, i.e. Reynolds numbers, with measurements taken at the same flow speed and streamwise position. The present data appear to follow a straight line in figure 21; however, it is not known whether each point would appear on a slightly different line if there were measurements at various streamwise positions for each flow condition.

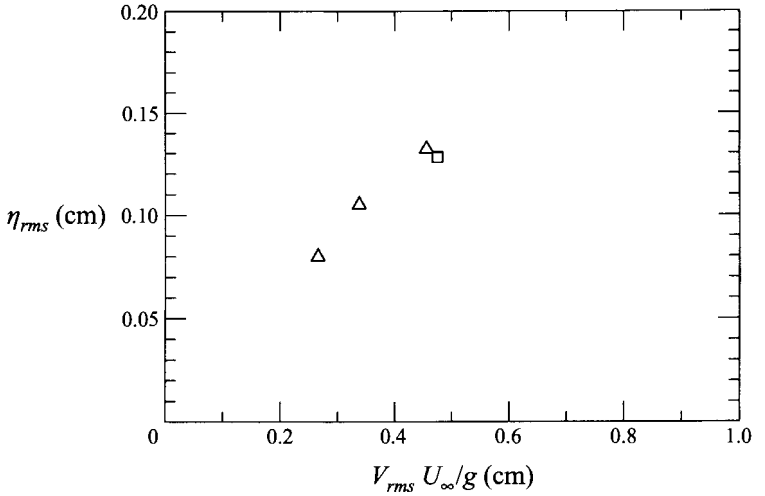

FIGURE 22. Plot of η_{rms} versus $V_{rms}U_\infty/g$ at the second trough of the following wavetrain. △, $U_\infty = 80$ cm s^{-1}; and □, $U_\infty = 100$ cm s^{-1}.

It is interesting to compare the Reynolds numbers of the present data to those of the data found in figure 2 of Wygnanski *et al.* (1986). To do this, an equivalent cylinder diameter must be determined for each breaking wave. Since D_T, U_∞, ν and ρ are known for the waves and curves of the drag coefficient, $C_d = 2D_c/\rho U^2 d_c$ (where $D_c \approx 2D_T$ is the drag on the cylinder and d_c is the diameter of the cylinder), versus Reynolds number, $U_\infty d_c/\nu$, are available in the literature, it is possible to compute equivalent values of d_c for each of the waves by iteration. The resulting Reynolds numbers are shown in table 3. These numbers range from 4400 to 11000 for the data plotted in figure 21 and is within the range of Reynolds numbers found in figure 2 of Wygnanski *et al.* (1986). However, the slope of the straight line fitted through the present data or the slope of any line drawn through one of the data points and the origin is less than the slope of any of the data sets in the cylinder data. That the present slopes are different than those of the cylinder data is not surprising since Wygnanski *et al.* (1986) showed the importance of the near-wake shear-layer instability to the details of the wake, and the shear-layer instability of the present flow at the breaker is greatly influenced by the free surface.

The last topic considered here is the relationship between η_{rms} and V_{rms}. In the above discussion, it has been found that the ripples in the wake are generated by instabilities of the shear layer in the breaking region and propagate over the wake like gravity waves on a current that is varying as $x^{-1/2}$. As a result, η_{rms} decreases as $x^{-1/2}$. The turbulent wake also originates at the breaker and its behaviour and characteristics are influenced by the instabilities of the same shear layer that generates the surface ripples. It has been established by Battjes & Sakai (1981) and Duncan (1981) that the turbulent wake of a breaker behaves like the wake of a two-dimensional body in an unbounded fluid. Therefore, even though only one measurement of V_{rms} was taken for each of four waves in the present experiments, it is expected that V_{rms} decreases as $x^{-1/2}$ in the present case as well. Given the above findings, one would expect the ratio of V_{rms}/η_{rms} to be constant in each wake. A plot of η_{rms} versus $V_{rms}U_\infty/g$ is shown in figure 22. The four data points, one point for each of the four breakers, form a nearly straight line. Thus, based on the small data set presented here and the known behaviour of η_{rms} and V_{rms}, it appears that the dimensionless ratio $(g\eta_{rms})/(U_\infty V_{rms})$

is the same constant in all the wakes and at any position in those wakes. The actual values of this ratio are shown in table 3 and have a mean value of 0.292 with a standard deviation of 5%.

5. Conclusions

Measurements of the mean and fluctuating surface profiles of steady breaking waves and their wakes, together with measurements of the vertical distribution of vertical and horizontal velocity fluctuations at a single station behind the breaking waves, have been presented. The spectrum of the surface ripples in the wake is highly peaked and shows little variation in shape or frequency over the first three wavelengths of the following wave. For a given speed, as the breaker strength is increased, the high-frequency ends of the spectra are nearly identical and follow a frequency to the $-7/2$ power law. The frequency of the spectral peak decreases and the r.m.s. ripple amplitude, η_{rms}, increases as either the breaker strength or the flow speed is increased. The physics of the ripple generation process was explored with a linear instability analysis of the shear flow at the breaking region, which is modelled with the mean velocity profile of the half-wake of a two-dimensional body in an unbounded fluid. The measured frequencies of the ripples in the wake, the wavelengths of the ripples at the breaker, the estimations of the momentum thickness for each wave (based on the correlations presented in §3.2), and the concept of the mean flow at the breaking region as a weak roller with a mean fluid speed at the free surface of about $-0.05U_\infty$ were found to be consistent with the results of the instability model. These results indicate that the surface ripples are generated by the shear flow at the breaking region. In the wake, η_{rms} decreases with distance, x, behind the breaker to the $-1/2$ power in agreement with wave action theory for waves propagating downstream from the breaker over a two-dimensional wake flow that varies as $x^{-1/2}$. The spectrum of the vertical velocity fluctuations was also found to be highly peaked with the same peak frequency as that of the ripples while the spectrum of horizontal velocity fluctuations was found not to be highly peaked. Since η_{rms} decreases as $x^{-1/2}$ and V_{rms} is expected to decrease as $x^{-1/2}$ in a two-dimensional wake, $(g\eta_{rms})/(U_\infty V_{rms})$ will be independent of x in a given breaker. In addition, the measurements show that $(g\eta_{rms})/(U_\infty V_{rms})$ is nearly constant (0.292 ± 0.015) for the breaking waves studied here.

The experiments reported herein were performed at Quest Integrated, Inc. in Kent, Washington by R. Srnsky and his staff and were supervised by Dr P. Liu. The authors wish to express their gratitude to B. Marasli for a number of helpful discussions during the analysis of the data. The support of the David Taylor Research Center under contract N00167-87-C-0092 and the Office of Naval Research under contract N00014-90-J-1977 is gratefully acknowledged.

REFERENCES

ANTHONY, D. G. & WILLMARTH, W.W. 1992 Turbulence measurements in a round jet beneath a free surface. *J. Fluid Mech.* **243**, 699–720.

BABA, E. 1969 A new component of viscous resistance. *J. Soc. Nav. Arch. Japan* **125**, 23.

BANNER, M. L. & FOOKS, E. H. 1985 On the microwave reflectivity of small scale breaking water waves. *Proc. R. Soc. Lond.* A **399**, 93–103.

BATTJES, J. A. & SAKAI, T. 1981 Velocity field in a steady breaker. *J. Fluid Mech.* **111**, 421–437.

CHEVRAY, R. & KOVASZNAY, S. G. 1969 Turbulence measurements in the wake of a thin flat plate. *AIAA J.* **7**, 1641–1643.

COINTE, R. & TULIN, M. P. 1994 A theory of steady breakers. *J. Fluid Mech.* **276**, 1–20.

DIMAS, A. A. & TRIANTAFYLLOU, G. S. 1994 Nonlinear interaction of shear flow with a free surface. *J. Fluid Mech.* **260**, 211–246.

DUNCAN, J. H. 1981 An experimental investigation of breaking waves generated by a towed hydrofoil. *Proc. R. Soc. Lond.* A **377**, 331–348.

DUNCAN, J. H. 1983*a* The breaking and non-breaking wave resistance of a two-dimensional hydrofoil. *J. Fluid Mech.* **126**, 507–520.

DUNCAN, J. H. 1983*b* A note on the evaluation of the wave resistance of two-dimensional bodies from measurements of the downstream profile. *J. Ship Res.* **27**, 90–92.

DUNCAN, J. H. 1993 Surface roughness in the wake of a steady breaking wave. *Proc. Third Intl Offshore and Polar Engng Conf.* **3**, 39–44.

KOMORI, S., UEDA, H., OGINO, F. & MIZUSHIMA, T. 1982 Turbulence structure and transport mechanism at the free surface in an open channel flow. *Intl J. Heat Mass Transfer* **25**, 513–521.

LIN, J.-C. & ROCKWELL, D. 1994 Instantaneous structure of a breaking wave. *Phys. Fluids* **6**, 2877–2879.

LIN, J.-C. & ROCKWELL, D. 1996 Evolution of a quasi-steady breaking wave. *J. Fluid Mech.* **302**, 29–44.

LIN, J.-T. & LIU, H.-T. 1982 On the spectra of high-frequency wind waves. *J. Fluid Mech.* **123**, 165–185.

LONGUET-HIGGINS, M. S. & STEWART, R. W. 1960 Changes in the form of short gravity waves on long waves and tidal currents. *J. Fluid Mech.* **8**, 565–583.

MARASLI, B., NGUYEN, P. & WALLACE, J. M. 1993 A calibration technique for multiple-sensor hot-wire probes and its application to vorticity measurements in the wake of a circular cylinder. *Exps. Fluids* **15**, 209–218.

MARCHMAN, J. F. & ABTAHI, A. A. 1985 Aerodynamics of an aspect ratio 8 wing at low Reynolds numbers. *J. Aircraft* **22**, 628–634.

MOLER, C. & STEWART, G. W. 1973 An algorithm for generalized matrix eigenvalue problems. *SIAM J. Numer. Anal.* **10**, 241–256.

PEREGRINE, D. H. 1976 Interaction of water waves and currents. *Adv. Appl. Mech.* **16**, 9–117.

PRESS, W., FLANNERY, B., TEUKOLSKY, S. & VETTERLING, W. 1986 *Numerical Recipes.* Cambridge University Press.

RASHIDI, M. & BANERJEE, S. 1988 Turbulence structure in free-surface channel flows. *Phys. Fluids* **31**, 2491–2503.

SWEAN, T. F., RAMBERG, S. E., PLESNIAK, M. W. & STEWART, M. B. 1989 Turbulent surface jet in channel of limited depth. *J. Hydraul. Engng* **115**, 1587–1606.

TRIANTAFYLLOU, G. S. & DIMAS, A. A. 1989 Interaction of two-dimensional separated flows with a free surface at low Froude numbers. *Phys. Fluids* A **1**, 1813–1821.

WALKER, D. T., LYZENGA, D. R., ERICSON, E. A. & LUND, D. E. 1996 Radar backscatter and surface roughness measurements for stationary breaking waves. *Proc. R. Soc. Lond.* A **452**, 1953–1984.

WYGNANSKI, I., CHAMPAGNE, F. & MARASLI, B. 1986 On the large-scale structures in two-dimensional, small-deficit turbulent wakes. *J. Fluid Mech.* **168**, 31–71.